water

MDPI

Article

Synthesis of Ce-La-Pr/Mn-O Ternary Oxide Composites via Co-Precipitation and Synergistic Photocatalytic Degradation of Cr(VI)

Xiujuan Feng [1,2,3,4,*] and Zebang Yu [1,2,4]

[1] School of Mines, China University of Mining and Technology, Xuzhou 221116, China
[2] Industrial Technology Innovation Center for Ecological Restoration of Industrial and Mining Sites, Petroleum and Chemical Industry, Xuzhou 221116, China
[3] Jiangsu Yuankun Rare Earth Co., Ltd., No.99, University Rd, High-Tech Industrial Development Zone, Xuzhou 221112, China
[4] Mechano Chemistry Research Institute, China University of Mining and Technology, Xuzhou 221116, China
* Correspondence: xjfeng@cumt.edu.cn or xiujuanf@126.com

Abstract: This study utilized a straightforward co-precipitation method to successfully synthesize Ce-La-X(Mn/Pr)-O composite materials for treating simulated hexavalent chromium (Cr(VI)) wastewater with distinctively porous and fluffy textures, along with tubular morphologies. Notably, Ce-La-Mn-O demonstrated a remarkable specific surface area of 96.2698 m^2/g, mesoporous architecture with a pore diameter of 6.9511 nm, and an impressive adsorption capacity of 88.79 mg/g. Under optimized conditions, specifically an initial Cr(VI) concentration of 20 mg/L, a Ce-La-Mn-O dosage of 0.8 g/L, a reaction temperature of 40 °C, an initial pH of 6, and with the application of simulated daylight, the removal rate of Cr(VI) exceeded 98% within 15 min. Even after three cycles, the removal rate was maintained at above 80%. Based on a comprehensive suite of morphological, structural, and performance characterizations, the introduction of Mn/Pr was found to modify the structure of Ce-La-O and enhance the synergistic interactions among the metals within the Ce-La-O framework. In addition, Ce-La-Mn-O exhibited superior visible light absorption properties and dual functionality for catalytic reduction and adsorption. All three materials were found to form -OH polar bond functional groups, converting it to Cr(III) and subsequently forming $Cr(OH)_3$. The Ce-La-X(Mn/Pr)-O composite materials provide a robust theoretical foundation for exploring the dual functional synergistic effects in the efficient removal of Cr(VI) from aqueous systems, indicating their vast potential for practical applications.

Keywords: co-precipitation method; Ce-La-Pr/Mn; ternary oxide composites; photocatalysis; degradation; wastewater treatment; Cr(VI)

Citation: Feng, X.; Yu, Z. Synthesis of Ce-La-Pr/Mn-O Ternary Oxide Composites via Co-Precipitation and Synergistic Photocatalytic Degradation of Cr(VI). *Water* **2024**, *16*, 1178. https://doi.org/10.3390/w16081178

Academic Editor: Mehrab Mehrvar

Received: 28 February 2024
Revised: 13 April 2024
Accepted: 17 April 2024
Published: 20 April 2024

1. Introduction

Chromium is the 16th-most toxic and carcinogenic substance, and it is mainly derived from industrial wastewater, causing surface water, groundwater, and soil pollution [1]. It generally exists in the form of trivalent chromium (Cr(III)) and hexavalent chromium (Cr(VI)) [2]. Small quantities of Cr(III) serve as essential nutrients for maintaining human health, whereas Cr(VI), as one of the toxic metal ions, exhibits toxicity that is a thousandfold greater than that of Cr(III) [3]. Cr(VI) has a long-term toxic effect on the ecological environment and can accumulate in the human body through food chain enrichment, which may lead to lung cancer, permanent brain injury, and other diseases [4]. Therefore, it is a great challenge to remove Cr(VI) from wastewater before discharge.

At present, in most research on removing metal ions from wastewater, adsorption and photocatalytic reduction technologies are widely and deeply applied because of their easy design, simple operation, and good efficiency in removing pollutants [5,6]. Aiming at

the existing foundation of removing metal ions, rare earth-based materials have attracted many researchers' attention because of their activity and high adsorption capacity [7,8]. Rare earth oxides such as lanthanum oxide (La_2O_3) and cerium oxide (CeO_2) usually have a high specific surface area and number of active sites, which can effectively remove Cr(VI) through adsorption and redox reactions [9]. CeO_2 is one of the richest and cheapest rare earth oxides, which has acid resistance and alkali resistance and will not elute when removing harmful substances from water [10,11]. The research shows that by doping atoms into the lattice of CeO_2, its surface properties, such as surface acidity and defect sites, can be effectively regulated, and then its adsorption behavior for pollutants can be affected [12]. At the same time, La is also an ideal doping element, which can change the surface properties of the catalyst, affect the periodic lattice structure, and adjust the charge state [13,14]. He et al. and Yi et al. have proved that the doping of La can enlarge the specific surface area, increase the active sites, enhance the pollutant degradation performance, and prolong the service life of photocatalytic electrodes [15,16]. Zhang et al. employed N-modified La-doped hierarchical carbon composites (LNPC) for the treatment of phosphate in water bodies [17]. However, the materials doped exclusively with Ce or La have the problems of insufficient photocatalytic activity and low absorption of visible light [18]. Kalidasan et al. and Arulkumar et al. have found that Mn element doping is an effective method to enhance the degradation efficiency, photocatalytic activity, and visible light absorption of photocatalysts [19,20]. Mjahed et al. and Mikolajczyk et al. and Li et al. discovered that doping with Pr significantly enhances the visible light absorption spectrum and photocatalytic performance of the composite material [21–23]. Therefore, this study introduces Mn/Pr into the Ce-La binary system to further increase its reduction–adsorption activity and absorption capacity for visible light.

In this study, Mn/Pr-doped Ce/-La oxide composites were prepared by co-precipitation method, and the reaction of Cr(VI) on the prepared nanocomposites and the factors affecting the adsorption performance and reducing property, such as surface morphology, specific surface area, pH, initial concentration, time, etc., as well as the reaction kinetics and removal mechanism, were discussed.

2. Materials and Methods

2.1. Materials

Commercially available analytical grade chemicals, including cerium nitrate hexahydrate ($Ce(NO_3)_3{\cdot}6H_2O$), lanthanum nitrate hexahydrate ($La(NO_3)_3{\cdot}6H_2O$), praseodymium nitrate hexahydrate($Pr(NO_3)_3{\cdot}6H_2O$), manganese nitrate($Mn(NO_3)_2$), ammonium hydroxide ($NH_3{\cdot}H_2O$), hydrochloric acid (HCl), sodium hydroxide (NaOH), sodium sulfate (Na_2SO_4), sodium chloride (NaCl), sodium bicarbonate ($NaHCO_3$), calcium chloride ($CaCl_2$), Zinc chloride($ZnCl_2$), potassium chloride (KCl), potassium dichromate standard solution ($K_2Cr_2O_7$, 0.1002 mol·L^{-1}), and diphenylcarbazide ($C_{13}H_{14}N_4O$) were supplied by Sinopharm Chemical Reagent Co., Ltd. (Shanghai, China). All solutions were freshly prepared with deionized water (18.2 MΩ cm) utilizing HCl (0.1 mol/L) and NaOH (0.1 mol/L)-adjusted pH values. The standard solution of $K_2Cr_2O_7$ was diluted with deionized water to prepare Cr (VI) stock solution (10–80 mg/L) to simulate wastewater.

2.2. Synthesis of Ce-La-X(Mn/Pr)-O Ternary Oxide Composites

Ce/La oxide composites were prepared using the co-precipitation method. The preparation method is as follows: 2.778 g of cerium nitrate hexahydrate, 0.693 g of lanthanum nitrate hexahydrate, and 0.385 g of praseodymium nitrate hexahydrate (or 0.21 mL of 50 wt Mn $(NO_3)_2$) were weighed into a 100 mL beaker, and 25 mL of deionized water was added, and then stirred with a glass rod to make the solution completely dissolved. Place the beaker on a magnetic stirrer, adjust the rotational speed to 400 r/min, and set the stirring time to 0.5 h. Put the mixed solution into a water bath at a temperature of 70 °C for 0.5 h, and then take it out. Then, 6 mL of 25% wt ammonia was slowly added to the reacted solution and crystallised for 3 h. The crystals were dried in a drying oven at 105 °C for

12 h.The dried crystals were ground to 250 mesh and then calcined in a muffle furnace.The calcination temperature is set to 2 h at 500 °C, 500 °C calcined for 4 h, 2 h at 200 °C, natural cooling at room temperature; composite material preparation is complete, then removed. The composite material was prepared, removed, put into a sample sealed bag, and kept in the shade for the test. The preparation process is shown in Figure 1.

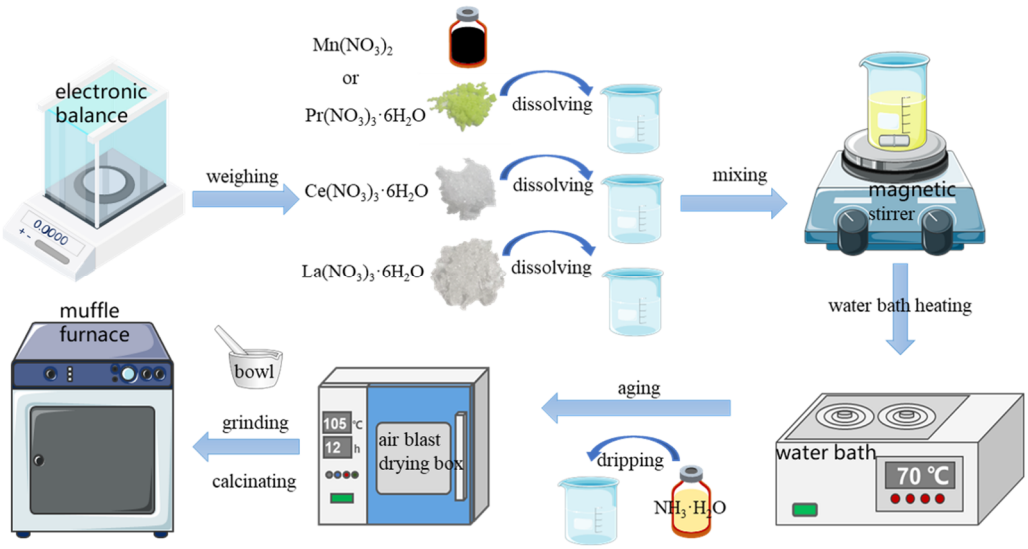

Figure 1. Ce-La-Pr and Ce-La-Mn preparation process schematic.

2.3. Material Characterization

The phase compositions of prepared raw powder and adsorbent material were characterized with X-ray diffraction (XRD, Empyrean, Panalytical, The Netherlands) with Cu Kα radiation at 40 kV and 40 mA in a scanning range of 10–80°. The morphology and microstructure of the sample were observed by scanning electron microscopy (SEM, Philips XL30 FEG, Amsterdam, The Netherlands) with an energy dispersive spectrometer (EDS). The functional groups were determined via Fourier transform infrared (FTIR) (Nicolet iS50 FTIR, Department of Physics, MDU) spectrophotometer in the wavenumber region of 500–4500 cm^{-1} before and after the reaction. The X-ray photoelectron spectrumetry (XPS, Thermo Fisher Scientific, Waltham, MA, USA) spectra were collected to analyze the surface compositions of the samples before and after reaction with Cr(VI). The surface properties of the raw powder and adsorption material prepared under the optimal process were determined using adsorption and desorption isotherms measured by an automatic specific surface area and pore size analyzer (ASAP2460, Micromeritics Instrument Corporation, Norcross, GA, USA) at −196 °C for physical adsorption of nitrogen. The two samples were degassed and dried at 105 °C in a vacuum for 12 h before testing. The Brunauer Emmett Teller (BET) isotherm was used to process the measured data in the relative pressure range of 0.1–0.25 to obtain each sample's specific surface area and micropore volume. The absorbance of the Cr(VI) solution was determined by an ultraviolet-visible spectrophotometer (UV-1800, Shanghai Meipuda Instrument, Shanghai, China) using dibenzoyl dihydrazide spectrophotometry. The concentration of the Cr(VI) solution was obtained according to the standard curve of absorbance and concentration. Considering that Cr(III) could appear in the solution after the reaction at lower pH, the total chromium content in the treated solutions was measured using the inductively coupled plasma spectrometer (ICP-OES, HKYT-799, Beijing Huakeyitong Analytical Instrument Co., Ltd., Beijing, China). The phase content and average grain size of the composite material were determined using image processing software (Image-Pro Plus, Version 7.0, Media Cybernetics, Bethesda, MD, USA) on SEM images.

2.4. Cr(VI) Removal Experiment

The experimental apparatus employed in this study comprised four integral components: a power supply, reactor, cooling system, and measurement system as shown in Figure 2. The light source consisted of a blue LED lamp with a central wavelength spanning from 420 nm to 840 nm. The reactor vessel was a 250 mL beaker situated on a magnetic stirrer, equipped with a rotor rotating to enhance the reaction kinetics. To prevent overheating and safeguard the lifespan of the light source, as well as ensure the safety of the experiment, a cooling fan was strategically positioned around the light source, serving as the cooling system. In each experiment, 0.04 g of Ce-La-X(pr/Mn)-O composite was added to 50 mL Cr(VI) solution, and the pH was adjusted to pH = 6 with 0.1 mol/L standard solution of hydrochloric acid. The temperature was 25 °C. We optimized the rotational speed to precisely 500 r/min, and the illumination was carried out by using a 300-watt xenon lamp with a wavelength of 420 nm for 120 min. At the end of the reaction, the solution was filtered using a 0.22 μm filter membrane, and the remaining concentration of Cr(VI) in the filtrate was measured using a spectrophotometer to calculate the removal rate of Cr(VI).

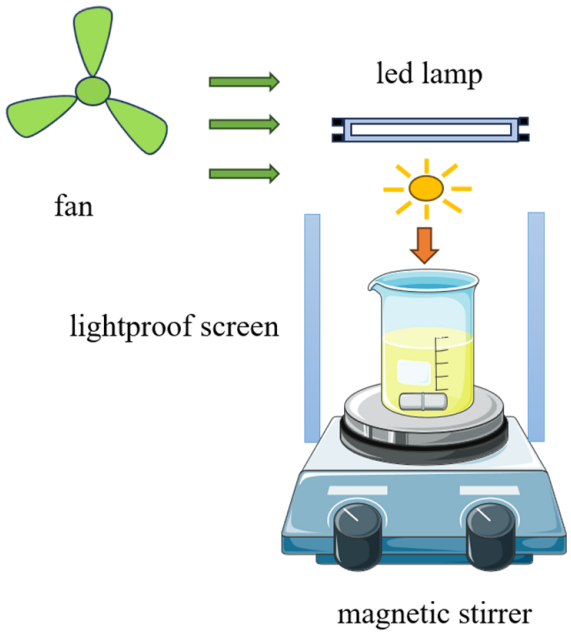

Figure 2. Reaction unit.

3. Results and Discussion

3.1. Crystal Structure, Morphology of Composites

In this study, we prepared three composite materials: Ce-La, Ce-La-Pr, and Ce-La-Mn-O, using identical experimental conditions. Analysis of the XRD patterns (Figure 3) revealed distinct characteristic diffraction peaks corresponding to the cubic fluorite structure of CeO_2 (JCPDS #34-0394) [24]. These peaks suggest a high degree of dispersion or weak crystallization of the active components. Compared to the standard CeO_2 card, the characteristic peaks of Ce-La-Pr and Ce-La-Mn shifted towards lower angles, particularly in regions such as the (111), (200), (220), and (311). Compared to Ce-La and Ce-La-Pr, the diffraction peaks in the sample were clearly visible on each corresponding crystal plane, but their intensities were significantly reduced, and the half-peak width was wider. This indicates a decrease in material crystallinity and grain size [25]. For Ce-La-Mn, when the doping levels of La and Mn are low, these elements primarily occupy lattice sites within CeO_2, replacing some Ce atoms. This substitution disrupts the crystal structure of CeO_2, leading to strong interactions between Ce, La, and Mn. Consequently, a Ce-O-Mn solid solution is formed, suppressing the growth of single crystals [26]. During the formation

of this solid solution, the incorporation of Mn ions with a smaller ionic radius into the CeO_2 lattice introduces lattice defects. These defects enhance the mobility of surface oxygen species and oxygen diffusion within the lattice, improving the material's catalytic properties [27]. The shift in the diffraction peaks of Ce-La-Mn indicates changes in the lattice parameters of the corresponding phase. This is attributed to the difference in ionic radii between the components of the composite material. Specifically, the radius of Ce (2.7 Å) is smaller than that of La (2.74 Å) but larger than that of Mn (1.79 Å). According to Bragg's equation ($2d\sin\theta = n\lambda$), the decrease in lattice parameters of Ce-La-Mn results from the incorporation of La and Mn into the CeO_2 lattice, leading to distortions in the cubic fluorite structure.

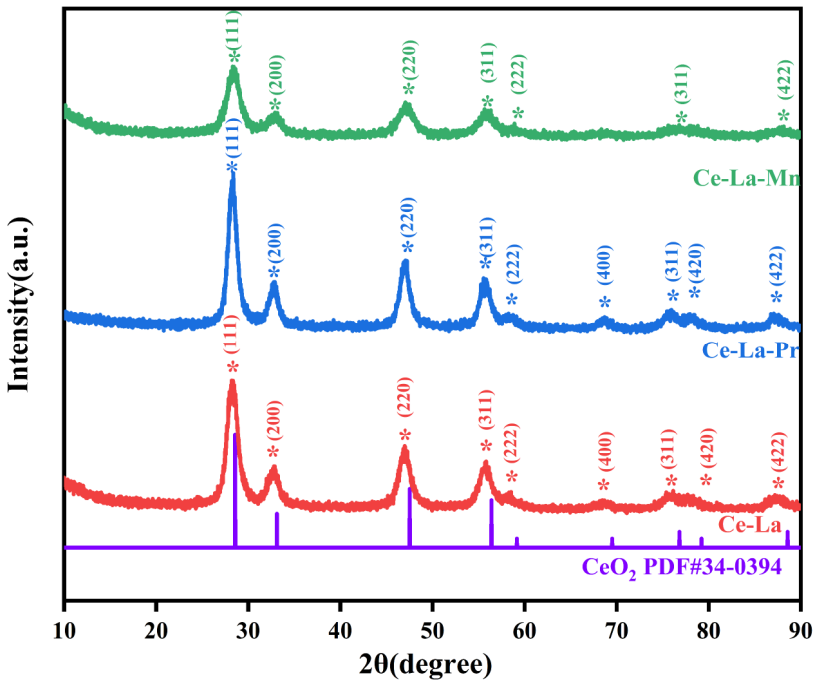

Figure 3. XRD patterns of Ce-La, Ce-La-Pr, Ce-La-Mn ("*" indicates the position of the characteristic peaks).

The specific surface area of the composite material affects the exposure rate of active sites and the diffusion process of reactants. Nitrogen adsorption–desorption isotherm tests were conducted on three composite materials under identical conditions (Figure 4). As shown in Figure 4a, all materials exhibited H_3 hysteresis loops, following the trend of IV-type isotherms. A higher adsorption capacity is observed at the high-pressure end, which is typically attributed to the formation of slit pores caused by the accumulation of platelet particles. The pore structure parameters of the three materials are presented in Table 1. The specific surface area of Ce-La-Mn calculated by BET is 96.2698 m^2/g, with a porosity of 0.167296 cm^3/g and a pore diameter of 6.9511 nm. Compared to Ce-La and Ce-La-Pr, there is a significant increase in both parameters, and all belong to the mesoporous structure. As seen in Figure 4b, the pore diameters of all three materials are within the range of 0–20 nm, indicating a mesoporous structure [28]. The introduction of Mn reduces the pore diameter to below 10 nm, indicating that Mn enhances the specific surface area of the Ce-La--based composite material to a greater extent. The large and irregular surface morphology of the porous structure provides more active sites for adsorption and reduction reactions. In summary, the doping of Mn makes Ce-La-Mn an ideal material for the removal of Cr(VI) in water purification.

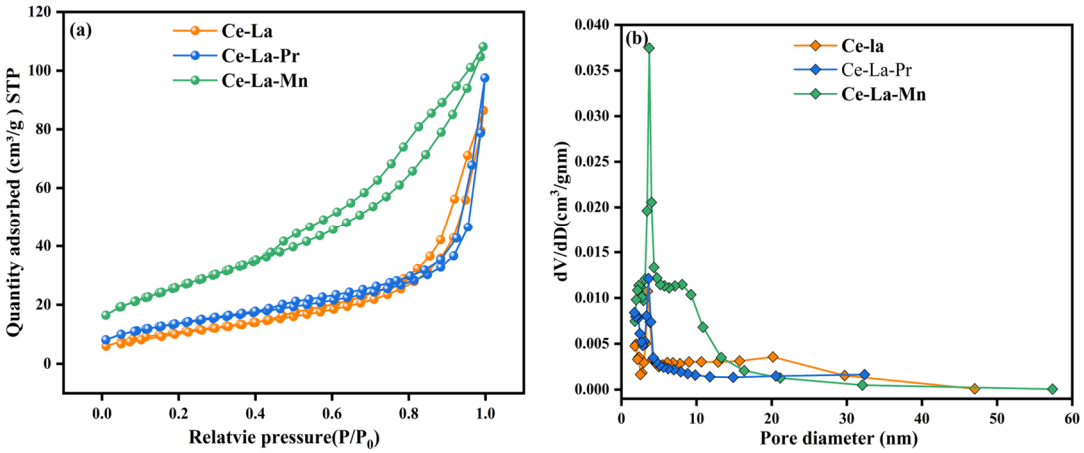

Figure 4. (**a**) N_2 adsorption–desorption isotherms of Ce-La and Ce-La-Pr and Ce-La-Mn; (**b**) pore size distribution curves of Ce-La and Ce-La-Pr and Ce-La-Mn.

Table 1. Structural properties of Ce-La and Ce-La-Pr and Ce-La-Mn.

Samples	S_{BET} (m^2/g)	V_{total} (cm^3/g)	P (nm)
Ce-La	39.3386	0.133710	13.5958
Ce-La-Pr	48.8215	0.150878	12.3616
Ce-La-Mn	96.2698	0.167296	6.9511

The SEM observations and microstructural analyses of Ce-La-Mn before Cr(VI) removal are presented in Figure 5. Compared to Ce-La and Ce-La-Pr, this material exhibits a rougher surface texture. Following the introduction of Pr/Mn into the Ce-La binary system, the average particle size of the prepared Ce-La-Pr/Mn composites decreased from 57.9 ± 15.0 nm to 25.6 ± 4.5/28.2 ± 5.1 nm compared to the binary system. The loosely packed structure of the material contributes to a larger specific surface area, smaller particles, and improved dispersion, all enhancing its activity for Cr(VI) removal [29]. XRD analysis revealed that the introduction of Pr/Mn into the CeLaOx lattice during preparation caused lattice distortion and the formation of a Ce-La-O-Pr/Mn solid solution. Notably, the incorporation of Mn results in stronger interactions between metal ions than Pr, leading to an increase in specific surface area and the generation of active sites. These characteristics favor the removal of Cr(VI) by the composite material.

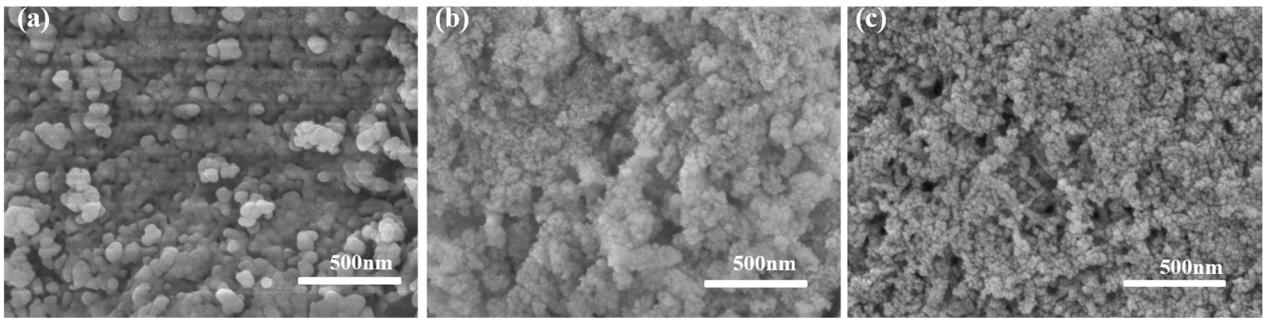

Figure 5. SEM images of (**a**) Ce-La, (**b**) Ce-La-Pr, and (**c**) Ce-La-Mn.

UV-Vis DRS spectroscopy was employed to investigate the light absorption characteristics of Ce-La-X(Mn/Pr) (Figure 6). Ce-La itself exhibits a strong absorption band in the ultraviolet region (400 nm), attributed to charge transfer during the O 2p to Ce 4f transition of Ce^{4+} and O^{2-} [30]. Upon doping with Pr and Mn, the light absorption capacity in the visible region (400–700 nm) is enhanced, resulting in a red shift in the absorption spectrum.

The absorption edges shift to approximately 600 nm and beyond 800 nm, respectively, with a significant increase in light absorption intensity above 400 nm. This enhancement is likely due to lattice defects and oxygen vacancies introduced by doping [9]. The increased visible light absorption generates more electron–hole pairs, favoring the photocatalytic reaction. The band gap sizes were estimated using the Kubelka–Munk equation:

$$\left(\alpha hv\right)^{1/n} = A\left(hv - E_g\right) \quad (1)$$

where α is the absorption coefficient, hv is the discrete photon energy, and A is a constant. The exponent n is related to the type of optical transition in the band gap. For direct band gap semiconductors, the exponent n equals 1/2, whereas for indirect band-gap semiconductors, it equals 2. Given that Ce-La-based composites exhibit indirect band-gap characteristics [31], an exponent of n = 2 was employed in our analysis. Based on these calculations, the band gaps of Ce-La, Ce-La-Pr, and Ce-La-Mn are 2.30 eV, 2.01 eV, and 1.91 eV, respectively. Mn doping results in a narrower optical band gap due to multi-body effects on the CB and VB, leading to stronger interactions between Ce, La, and Mn, higher rates of photogenerated electron—hole separation, and a broader photoresponse range [32]. Collectively, these findings indicate that Ce-La-Mn has a suitable band gap and excellent photocatalytic reduction ability for Cr(VI) under visible light irradiation.

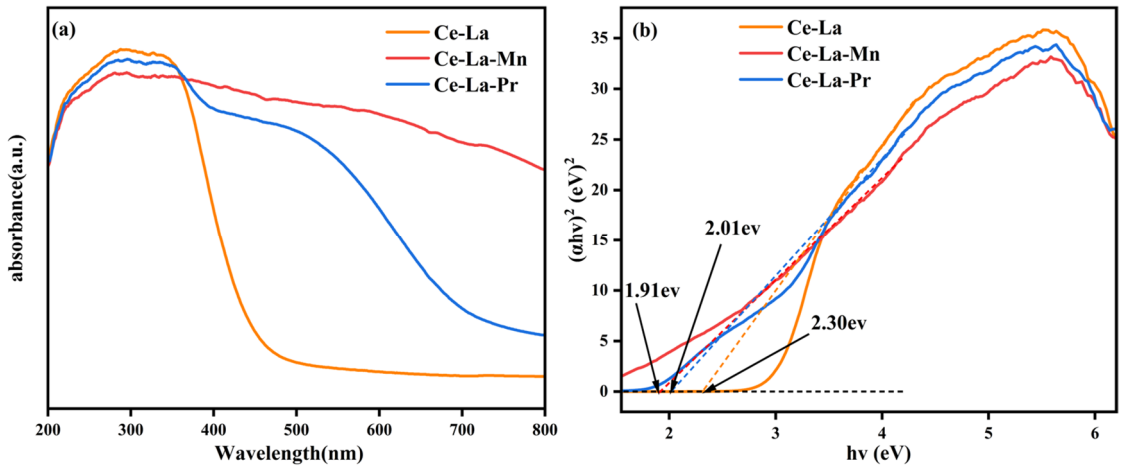

Figure 6. (**a**) UV-VisDRS (UV-vis Diffuse Reflection Spectroscopy) of Ce-La-Mn, Ce-La-Pr and Ce-La; (**b**) Tauc plot of Ce-La-Mn, Ce-La-Pr and Ce-La. The dotted lines depict the linear segment of the Tauc plot.

3.2. Cr(VI) Removal Test

Figure 7a illustrates the impact of dosage on the removal of Cr(VI) from aqueous media by composite materials. Analysis of the figure reveals that the removal efficiency of Cr(VI) by the three composite materials increases with increasing dosage, and the increment in removal rate diminishes when the dosage exceeds 0.14 g. This phenomenon can be explained by the fixation process of Cr(VI) reactions, where Cr(VI) initially diffuses from the solution onto the surface of the composite materials. Subsequently, with the transfer of electrons from the Ce, La, Mn/Pr cores, Cr(VI) is reduced to Cr(III), which then precipitates or adsorbs onto the surface of the materials. At lower dosages, the stronger driving force for Cr(VI) diffusion and the limited active sites on the composite materials prolong the fixation time of Cr(VI), leading to increased reaction time and a slower reaction rate. This is attributed to the decrease in solute flux or concentration gradient within the solution, or the concentration difference between the solute in the solution and the composite material surface. The removal efficiency of Cr(VI) by the three composite materials gradually enhances with an increase in dosage. The incremental increase in removal efficiency becomes marginal beyond a dosage of 0.14 g.

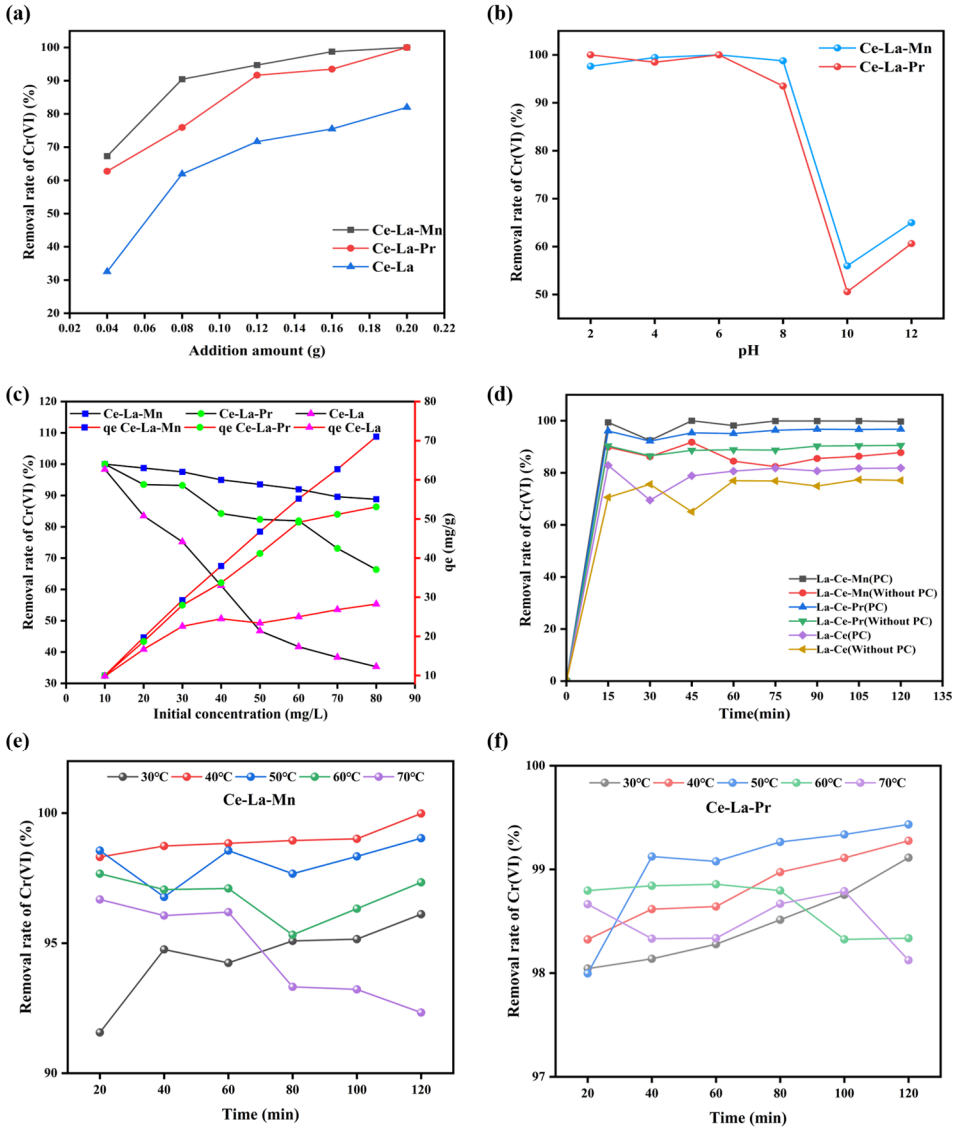

Figure 7. (**a**) Effect of addition amount on catalyst performance, experimental conditions: Cr(VI) = 20 mg/L, pH = 6, T = 25 °C, photocatalysis; (**b**) Effect of pH on catalyst performance, experimental conditions: Cr(VI) = 20 mg/L, absorbent = 0.04 g, T = 25 °C, photocatalysis; (**c**) Effect of initial concentration on catalyst performance, experimental conditions: absorbent = 0.04 g, pH = 6, T = 25 °C, photocatalysis; (**d**) Effect of Photocatalytic conditions on catalyst performance, experimental conditions: Cr(VI) = 20 mg/L, absorbent = 0.04 g, pH = 6, T = 25 °C; (**e**,**f**) Effect of temperature on catalyst performance, experimental conditions: Cr(VI) = 20 mg/L, absorbent = 0.04 g, pH = 6, photocatalysis.

The impact of reaction pH on the removal of Cr(VI) from aqueous media by composite materials was recorded in Figure 7b. At a pH of 6, Ce-La-X(Mn/Pr) demonstrates the highest removal efficiency, achieving 100% removal. Nevertheless, under strongly acidic conditions (pH 2–4), the removal rate exhibits a marginal decrease. This can be attributed to the inability of the reduction product Cr(III) to deposit onto the surface of Ce-La-X composite materials through the formation of Cr(OH)x compounds, which is influenced by acid–base neutralization [33]. Ce-La-X can utilize its oxygen storage capacity and form more hydrogen bonds with $HCrO_4^-$ under acidic conditions. Furthermore, the presence of H^+ ions in the solution promotes their adsorption onto the surface of the composite material, thereby enhancing the electrostatic adsorption of $HCrO_4^-$. As the pH gradually rises in alkaline conditions, the removal rate decreases significantly. This is presumably attributed

to interactions between CrO_4^{2-} and OH^-, which gradually enhance electrostatic repulsion between Cr(VI) and the adsorbent, subsequently leading to a decrease in adsorption capacity and efficiency. Moreover, the photocatalytic reduction process of Cr(VI) by the material is influenced by the acidity or alkalinity of the system.

Acidic conditions:

$$Cr_2O_7^{2-} + 14H^+ + 6e^- = 2Cr^{3+} + 7H_2O;\ E^\theta = (Cr_2O_7^{2-}/Cr^{3+}) = 1.3\ V\ vs.\ NHE \quad (2)$$

Alkaline conditions:

$$CrO_4^{2-} + 4H_2O + 3e^- = Cr(OH)_3 + 5OH^-;\ E^\theta = (CrO_4^{2-}/Cr(OH)_3)^- = -0.13\ V\ vs.\ NHE \quad (3)$$

By the Nernst's equation:

$$E = E^\theta + \frac{RT}{6F}\ln\frac{\left[Cr_2O_7^{2-}\right]\cdot\left[H^+\right]^{14}}{\left[Cr^{3+}\right]^2} \quad (4)$$

$$E = E^\theta + \frac{RT}{3F}\ln\frac{\left[CrO4^{2-}\right]}{\left[OH^-\right]^5} \quad (5)$$

Based on the Nernst Equation, an increase in the concentration of H^+ leads to an elevation in the electrode potential of the $Cr_2O_7^{2-}/Cr^{3+}$ couple, favoring the reaction proceeding from left to right and thereby increasing the rate of Cr(III) formation. Conversely, as the concentration of OH^- increases, Cr(III) precipitates as $Cr(OH)_3$, occupying effective photocatalytic active sites and thereby decreasing photocatalytic performance. Furthermore, the decreased electrode potential of $CrO_4^{2-}/Cr\ (OH)_3$ significantly reduces the driving force for the photocatalytic reaction, making it insufficient to promote the reaction and, thus, more difficult for Cr(VI) to be reduced.

Figure 7c demonstrates the impact of initial Cr(VI) concentration on the removal of Cr(VI) by composite materials. Both Ce-La and Ce-La-Mn exhibit a decreasing removal rate with increasing concentration. Notably, Ce-La-Mn, incorporating Mn, experiences a less pronounced decrease. This is attributed to the reduction of active sites with rising ion concentration [34]. At higher Cr(VI) concentrations, intraparticle diffusion spreads the adsorbate across the adsorbent surface, leading to a further decrease in removal rate [35]. Mn introduction in Ce-La-Mn causes lattice distortion due to smaller ionic radius of Mn^{3+}, resulting in smaller grains, increased surface area, and more active and adsorption sites [36]. All materials show an increase in adsorption capacity with higher Cr(VI) concentrations. Ce-La rises from 9.83 mg/g to 35.32 mg/g, Ce-La-Pr from 9.99 mg/g to 66.35 mg/g, and Ce-La-Mn from 10 mg/g to 88.79 mg/g. This increase suggests more active sites become available with increasing metal concentration. The introduction of a third element significantly enhances the adsorption and catalytic reduction capabilities of Ce-La-based composites.

Figure 7d demonstrates the photocatalytic impact on Cr(VI) removal by Ce-La-Mn composites in aqueous solutions. Without photocatalysis, Ce-La-Mn removes Cr(VI) at 87.78%, exceeding Ce-La but trailing Ce-La-Pr. During the reaction, a decline in removal is observed after 45 min, followed by an increase at 75 min, stabilizing below the optimal rate. Introduction of photocatalysis elevates Cr(VI) removal to 99.79%, surpassing Ce-La-Pr and Ce-La. This improvement reflects a significant boost in photocatalytic efficiency. The light absorption is attributed to charge transition from the valence to conduction band. Mn doping enhances carrier migration on the composite surface, promoting electron trapping and photocatalytic activity [37]. The synergistic effect of Ce, La, and Mn tunes the composite's band structure and optical properties, suppressing electron–hole recombination. Traditional rare earth composites absorb limited visible light due to UV-biased band structures [9]. Ce-La's quantum confinement limits visible light absorption. Mn doping, with its unique

electronic structure, enables visible light absorption. Mn's 3d electron levels interact with the composite's bands, creating a new band structure, enhancing Cr(VI) reduction [38].

Figure 7e,f depict the impact of reaction temperature on Cr(VI) removal from aqueous solutions using Ce-La-Mn and Ce-La-Pr composites. As shown in Figure 7e, the removal rate of Cr(VI) by Ce-La-Mn increases initially with temperature, peaking at 50 °C. Subsequently, as the reaction proceeds, the removal rate of Cr(VI) by Ce-La-Mn increases with temperature in the range of 30–40 °C. However, with further increases in temperature from 40–70 °C, the removal rate decreases, achieving an optimal removal rate of 99.99% at 40 °C. This suggests that within the range of 30–40 °C, the elevated temperature enhances the adsorption and reduction capabilities of Ce-La-Mn for Cr(VI), providing greater possibilities for effective collisions between molecules and accelerating the reaction rate, and thus increasing the removal rate [39]. However, above 40 °C, a reduction in active sites and surface area leads to a decrease in the removal rate. Conversely, Ce-La-Pr achieves an optimal removal rate of 99.43% at 50 °C. The decrease in removal rate may be attributed to the reduction of active sites and surface area, resulting in a loss of activity for the composite material, preventing further reactions. Given the typical temperature range of Cr(VI)-related industrial wastewater (5–40 °C), Ce-La-Mn's broad temperature adaptability highlights its potential for industrial applications without additional temperature treatment.

Figure 8a illustrates the impact of reaction time on the removal of Cr(VI) from aqueous solutions by the composite materials. Analysis of the figure reveals that Ce-La-Mn, Ce-La-Pr, and Ce-La all achieve their optimal removal rates within the first 15 min of the 120-min reaction period. A slight decrease is observed at 30 min, followed by an increase at 45 min, gradually stabilizing around the optimal removal rate. This behavior can be attributed to the initial abundance of active sites and high solute gradient. As the adsorption process proceeds, however, the available active sites on the adsorbent surface gradually decrease, slowing down the adsorption rate of heavy metal ions. With further increases in reaction time, surface diffusion or internal migration of some adsorbed heavy metal ions within the composite material may occur, forming complex structures that reduce competition for active sites and promote the formation of new adsorption sites [40]. Consequently, the removal rate may increase again as the reaction time prolongs. Eventually, a dynamic equilibrium is reached between the adsorption and desorption of heavy metal ions, resulting in a stable removal rate. The local enlarged view shows that under identical reaction conditions, Ce-La-Mn exhibits superior removal rates compared to Ce-La-Pr and Ce-La, demonstrating the universality of this doping method and the further enhancement of Ce-La-based ternary composite performance.

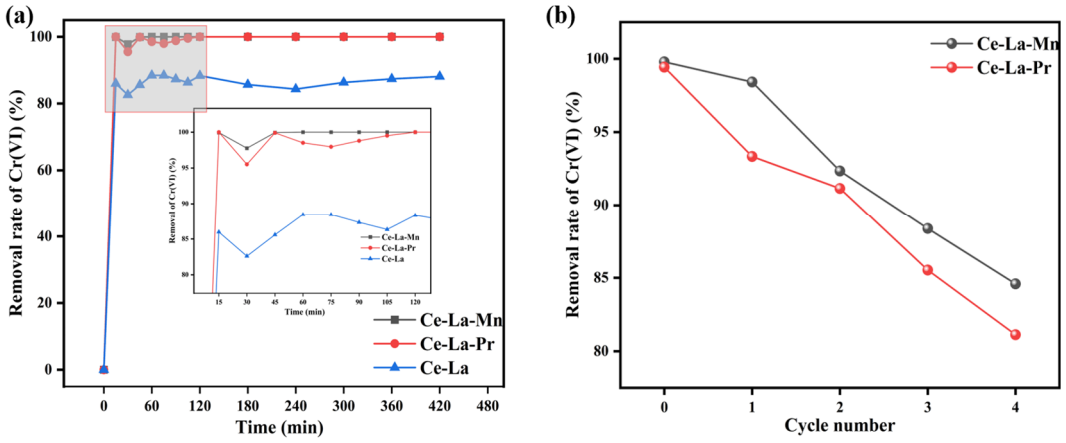

Figure 8. (**a**) Effect of addition amount on catalyst performance, experimental conditions: Cr(VI) = 20 mg/L, absorbent = 0.04 g, pH = 6, T = 25 °C, photocatalysis; (**b**) Cyclic regeneration test, experimental conditions: Cr(VI) = 20 mg/L, absorbent = 0.04 g, pH = 6, T = 25 °C.

The reusability, stability, and cost-effectiveness of materials are crucial in wastewater treatment, serving as key factors for the practical application of composites. To assess these properties, adsorption–desorption cycling experiments were conducted. Under the same experimental conditions as mentioned earlier, the filtered composites were immersed in 50 mL of 0.1 mol/L NaOH solution for 3 h. Subsequently, they were rinsed with deionized water until the pH was neutral, a process repeated twice before being placed in an oven at 85 °C for 12 h to dry. The dried material was then reused for the subsequent cycle. This cycling process was repeated.

The results are presented in Figure 8b. As evident from the figure, repeated cycling leads to a gradual decrease in Cr(VI) removal efficiency for both Ce-La-Mn and Ce-La-Pr. However, even after three cycles, the removal rate remains above 80%, indicating high recyclability, stability, and performance retention of these materials. This demonstrates their potential for practical applications.

Analysis of Figure 9a,c reveals the impact order of anions on Cr(VI) removal by Ce-La-X is Cl^- < SO_4^{2-} < HCO_3^-. Cl^- has lower binding energy and competes less with Cr(VI) for adsorption sites. An increase in HCO_3^- and SO_4^{2-} concentrations enhances Cr(VI) removal, possibly due to ion competition adsorption suppressing its adsorption and reduction [41]. Lower concentrations favor adsorption of these ions, while higher concentrations slightly improve photocatalytic Cr(VI) reduction. Figure 9b,d indicate the cations' influence on Cr(VI) removal: K^+ < Ca^{2+} < Zn^{2+}. Zn^{2+} forms a milky precipitate, indicating its high oxidation level and chemical instability, competing with Cr(VI) for reaction sites [42]. Zn^{2+}'s larger ion radius compared to K^+ and Ca^{2+} enhances its impact on Cr(VI) removal. However, this study considers only single ions; in practical applications, the combined presence of multiple ions complicates adsorption and requires further investigation.

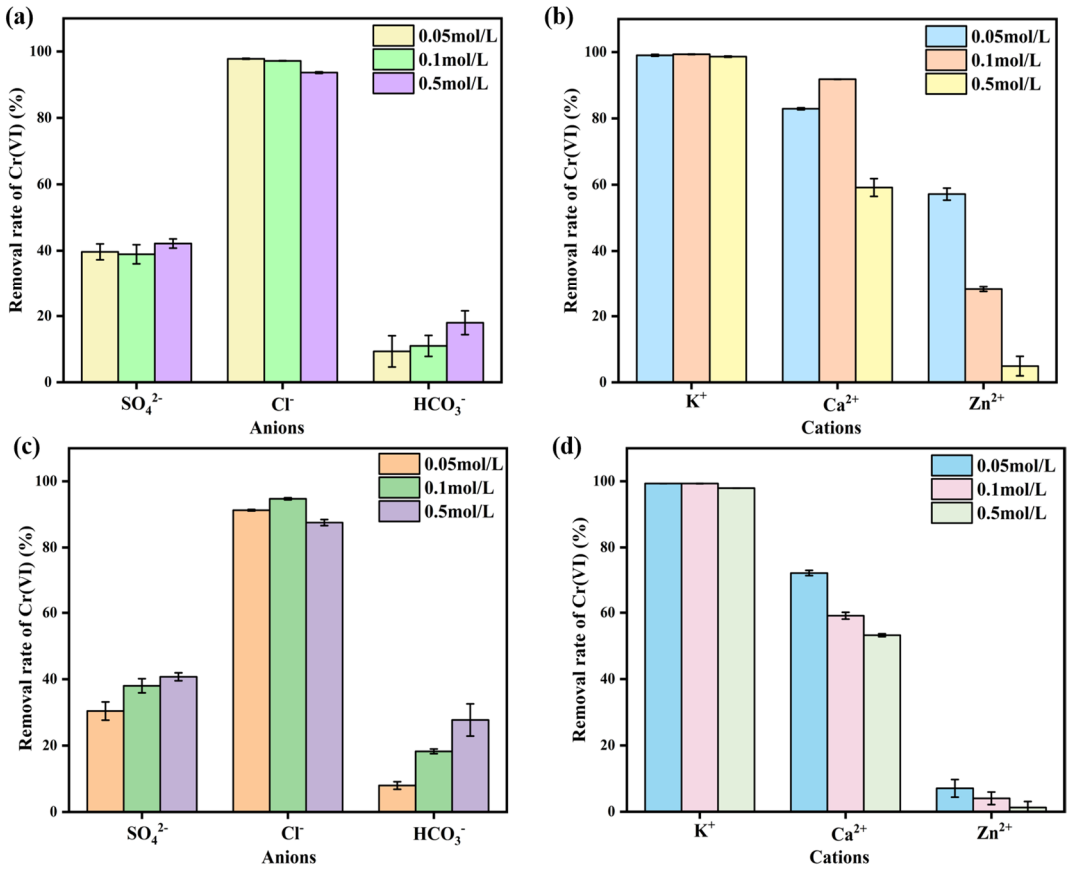

Figure 9. (**a**) Effect of anions on Ce-La-Mn performance; (**b**) Effect of cations on Ce-La-Mn performance; (**c**) Effect of anions on Ce-La-Pr performance; (**d**) Effect of cations on Ce-La-Pr performance. Experimental conditions: Cr(VI) = 20 mg/L, absorbent = 0.04 g, pH = 6, T = 25 °C, photocatalysis.

3.3. Reaction Kinetics

Reaction kinetics is an important factor to evaluate the Cr (VI) removal performance of composite materials. In this study, a quasi-first-order kinetic model was used to preliminary investigate the reaction kinetics of Ce-La-X (Mn/Pr). Fit according to Equations (6) and (7):

$$\log(q_e - q_t) = \log q_e - \frac{K_1 t}{2.303} \tag{6}$$

$$\frac{t}{q_t} = \frac{1}{K_2 q_e^2} + \frac{t}{q_e} \tag{7}$$

In the reaction equations, q_e represents the equilibrium concentration of Cr(VI) adsorbed (mg/g), while q_t denotes the concentration at any time t (min). K_1 and K_2 are the pseudo-first-order and pseudo-second-order rate constants (min^{-1}), respectively. The experimental results at different temperatures were fitted with both models, and the findings are presented in Figure 10 and Table 2. Both models showed strong linearity ($R^2 > 0.91$), with the pseudo-second-order model exhibiting the best fit ($R^2 > 0.9998$). This model suggests strong interactions or multiple reaction steps in Cr(VI) removal by Ce-La-X, indicating its suitability for describing the reaction kinetics.

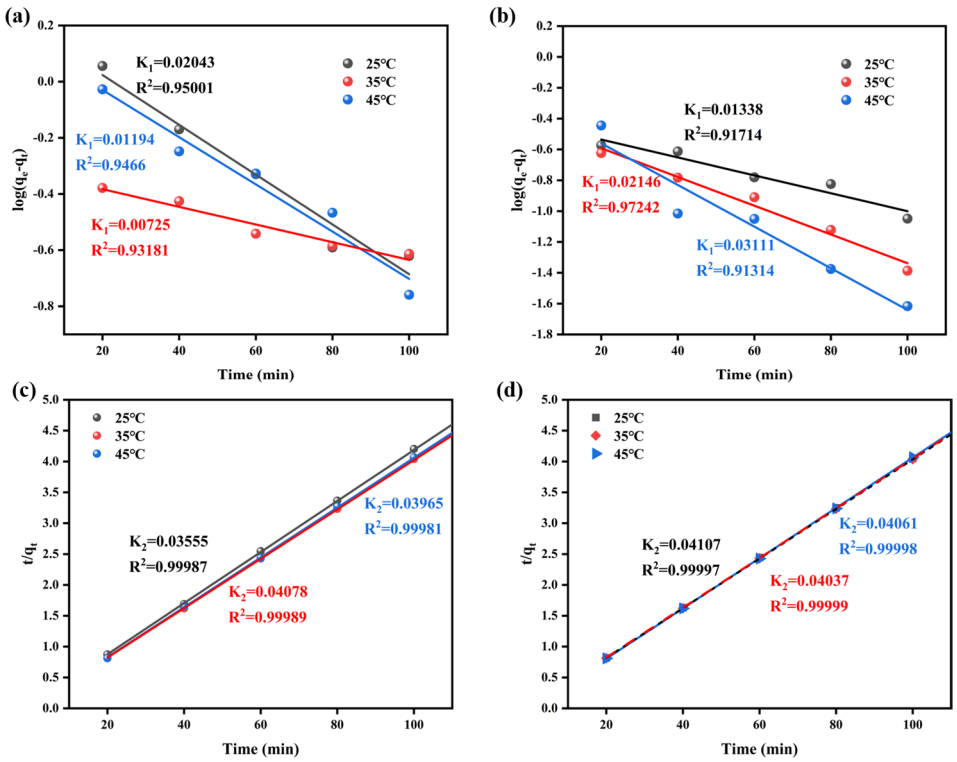

Figure 10. (**a**) Pseudo-first-order model of Ce-La-Mn and (**b**) Ce-La-Pr; (**c**) Pseudo-second order kinetics model of Ce-La-Mn and (**d**) Ce-La-Pr.

Table 2. Kinetic parameters of Cr (VI) removal by Ce-La-Pr and Ce-La-Mn.

Temperature		25 °C	35 °C	45 °C
Pseudo-First-Order Kinetics model Ce-La-Mn	K_1	0.02043	0.00725	0.01194
	R^2	0.95001	0.93181	0.94660
Pseudo-second-order kinetic model Ce-La-Mn	K_2	0.03555	0.04078	0.03965
	R^2	0.99987	0.99989	0.99981
Pseudo-first-order kinetic model Ce-La-Pr	K_1	0.01338	0.02146	0.03111
	R^2	0.91714	0.97242	0.91314
Pseudo-second-order kinetic model Ce-La-Pr	K_2	0.04107	0.04037	0.04061
	R^2	0.99997	0.99999	0.99998

3.4. Reaction Mechanism

To elucidate the reaction mechanism of the composite material, the morphology, valence state, element distribution, and content were analyzed before and after the reaction.

Figure 11 shows the SEM images of Ce-La-Mn after its reaction with Cr(VI). The post-reaction surface exhibits a roughened texture with numerous fine, irregular particles, which obstruct the pore structure and result in a blurred edge and reduced specific surface area. This indicates a successful interaction with Cr(VI) in the aqueous environment. The EDS-Mapping analysis of the reacted composite reveals a uniform distribution of Ce, La, Mn, O, and Cr on its surface. Quantitative analysis (Table 3) confirms that O dominates, while the atomic ratios of Ce/La (4.09) and Ce/Mn (7.37) closely align with the original molar ratios used in its preparation (4:1 and 0.72:1). Together, these observations confirm the successful incorporation of Cr into the composite material.

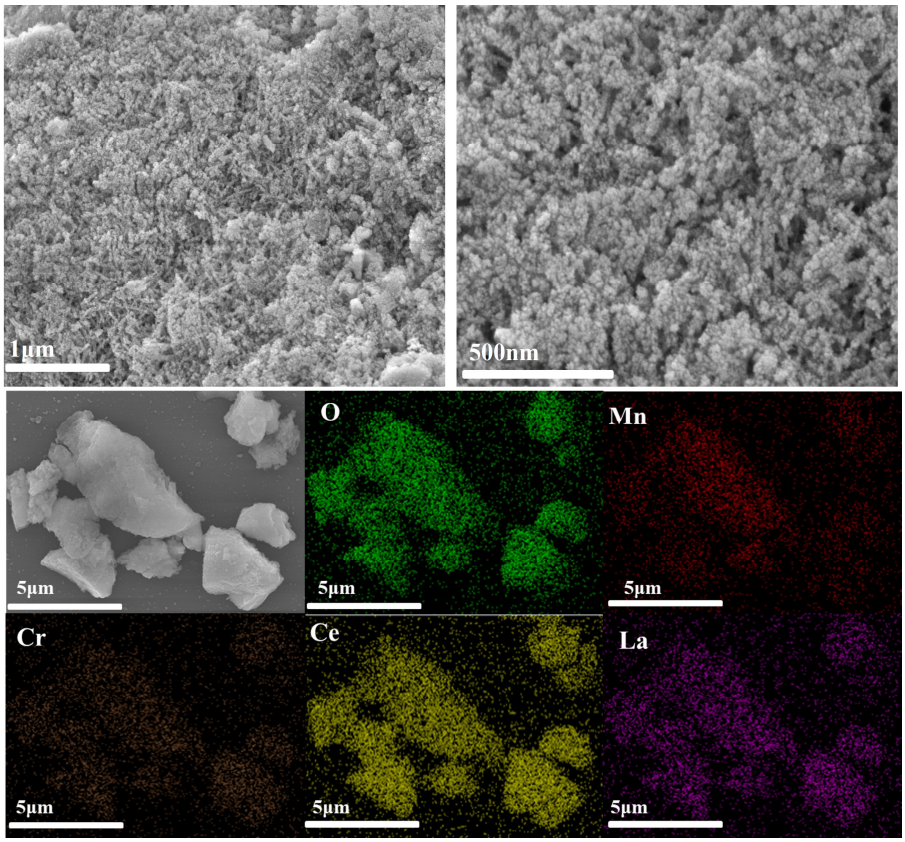

Figure 11. SEM images and elemental mapping of Ce-La-Mn after reaction.

Table 3. Element content table.

Element	Wt%	At%
O	30.46	75.39
Ce	49.95	17.55
La	12.32	4.29
Mn	6.84	2.38
Cr	0.43	0.39

The FTIR results (Figure 12) indicate that the presence of hydroxyl groups at 3427 cm^{-1} and a feature peak at 850 cm^{-1} [43], which remains unchanged in the three Ce-La-based composites after the reaction, suggest that the removal of Cr(VI) is related to the presence of hydroxyl groups on the surface of the composites. Chromate ions are adsorbed onto the composite surface through hydrogen bonding with -OH groups, which serve as one

of the main functional groups involved in the adsorption process [44]. Among the three composite oxides, the Ce-La-O oxide exhibits the most prominent characteristic peak, indicating a higher content of -OH groups in the following order: Ce-La-O > Ce-La-Mn-O > Ce-La-Pr-O. The -OH group, being a charged polar group, can undergo redox reactions. Coupled with the catalytic effect of CeO_2, it generates $Cr(OH)_3$. The bending vibration characteristic peaks of Ce-OH and La-OH, as well as the peak at 1055 cm^{-1}, exhibit blue shifts. The stretching vibrations of Ce-O, La-O, and Mn-O bonds lead to red shifts in their characteristic peaks. The decreased peak intensity after the reaction further indicates the adsorption and reduction of Cr(VI). Due to differences in the electronic structure and bonding states of Ce, La, Mn, and Pr in the oxides, their mixing may lead to electron transfer and rearrangement, affecting the vibration frequencies of chemical bonds and resulting in shifts in the characteristic peaks. This may also give rise to new reaction intermediates or products compared to the original binary composites. Additionally, the introduction of the doping element Mn appears to enhance the reaction efficiency, resulting in more Cr(VI) being adsorbed onto the composite surface and reduced to Cr(III).

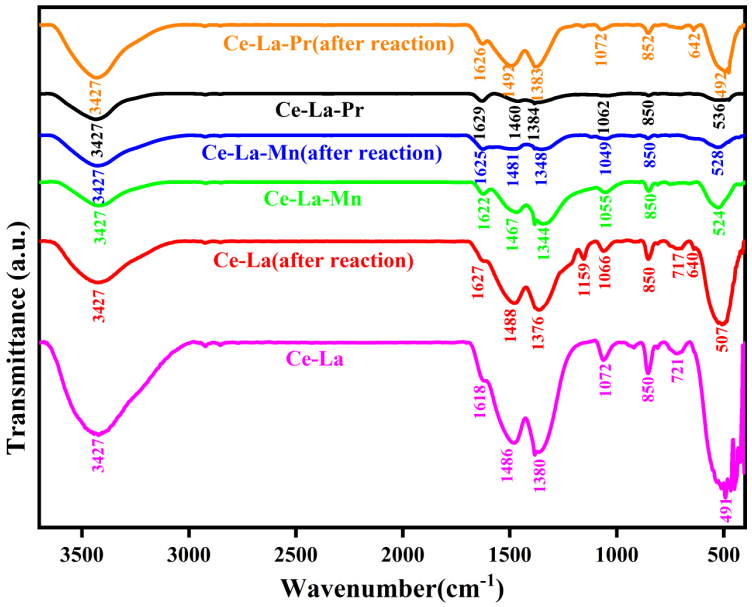

Figure 12. FTIR results of Ce-La-Mn and Ce-La-Mn (after reaction).

Variations in pH affect the Zeta potential, as shown in Table 4 and Figure 13. Ce-La-Mn has a pHZPC (point of zero charge) of 3.3, which is lower than Ce-La-Pr's, suggesting that Ce-La-Mn has a stronger acidic character, providing more active sites and acidic environments conducive to the reduction of Cr(VI) ions. Under acidic conditions, Cr(VI) ions are more likely to be reduced to trivalent chromium ions, reducing their toxicity. Moreover, negative charges resulting from the dissociation of surface functional groups like -OH and -COOH repel negatively charged chromate ions, preventing their adsorption at high pH values. As pH decreases, surface functional groups protonate and become positively charged, conferring a positive charge on the Ce-La-Mn surface. The positive charge strongly attracts chromate anions, and unstable $HCrO_4^-$ or $Cr_2O_7^{2-}$ ions are more prone to occupying adsorption sites and absorbing photons for reduction under weakly acidic conditions. Consequently, a higher removal rate of chromate is observed in weakly acidic environments.

Table 4. Zeta potential.

pH	3	5	6	7	9	11
Zeta potential (Ce-La-Pr)	30.3	11.96	0.38	1.28	3.97	9.14
Zeta potential (Ce-La-Mn)	2.53	−6.80	−7.71	−8.37	−12.00	−18.35

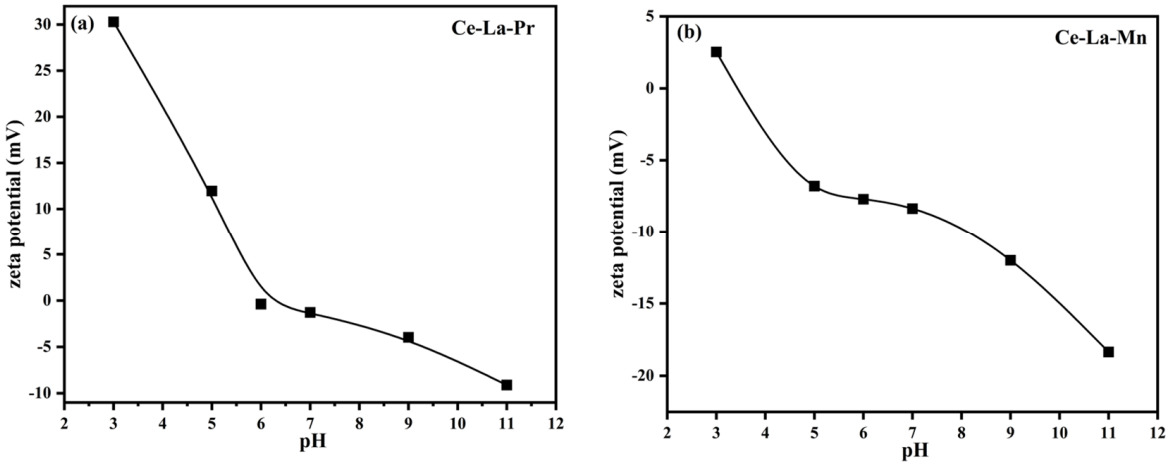

Figure 13. (**a**) The Zeta potential of Ce-La-Pr and (**b**) Ce-La-Mn at different pH.

Figure 14a presents the XPS spectra of Ce 3d for Ce-La-Mn before and after the reaction. The symmetry of the spectra for both the unreacted and reacted Ce-La-Mn is poor. When fitted according to the Ce 3d orbital peaks, the spectra can be divided into two regions corresponding to Ce $3d_{5/2}$ (881–897 eV) and Ce $3d_{3/2}$ (898–917 eV). The Ce 3d orbitals produce spin-orbit splitting, resulting in multiple peaks. The letters U and V represent the spin-orbitals of $3d_{3/2}$ and $3d_{5/2}$, respectively. After the reaction, the proportion of Ce(IV) in the Ce-La-Mn catalyst decreased from 89.47% to 72.60%, while the proportion of Ce(III) ions increased from 10.53% to 27.4%. This indicates that Ce exists in both Ce(III) and Ce(IV) valence states in the composite material, with the majority of Ce being in the Ce(IV) state. During the reaction, a significant amount of Ce(IV) gains electrons and undergoes an ionic reaction to convert to Ce(III), thereby enhancing the adsorption and photocatalytic activities of the composite material and improving its removal efficiency [45].

Figure 14b presents the XPS spectra of O 1s for the composite material before and after the reaction. When fitted according to the O 1s peaks, the spectra can be divided into three regions between 528 eV and 534 eV: lattice oxygen (Olatt) at 529 eV, oxygen vacancies (Ovs) at 531–532 eV, and adsorbed oxygen (Oads) predominantly in the form of -OH above 533 eV [46]. After the reaction, most of the lattice oxygen and all of the adsorbed oxygen were converted into oxygen vacancies. The proportion of lattice oxygen decreased from 55.08% to 49.87%, while the oxygen vacancies increased from 40.88% to 49.87%. A higher concentration of lattice oxygen is beneficial for enhancing the photocatalytic performance of the composite material. Compared to Ce-La-Pr, Ce-La-Mn exhibits a higher conversion rate of oxygen vacancies, indicating superior performance. This is consistent with the trend in the activity of the composite material.

Figure 14c displays the XPS spectra of Mn $2p_{3/2}$ for the composite material before and after the reaction. When fitted according to the Mn $2p_{3/2}$ peaks, three peaks can be observed between 635 eV and 650 eV due to the shake-up effect and the presence of multiple split peaks. These peaks, in order of increasing binding energy, correspond to Mn(II), Mn(III), and Mn(IV). Before the reaction, the composite material contained Mn(II) at 33.33%, Mn(III) at 54.12%, and Mn(IV) at 12.55%. After reacting with Cr(VI), the proportion of Mn(II) decreased to 13.16%, while Mn(III) increased to 73.42% and Mn(IV) increased to 13.48%.

This indicates that during the reaction, a significant amount of Mn(II) was converted to the higher oxidation state of Mn(III), while a smaller portion was converted to Mn(IV). The appearance of oxidized Mn species after the reaction suggests a correlation between the reduction of Cr(VI) and the oxidation of Mn to higher states. This suggests that doping Mn into Ce/La oxides facilitates the formation of Cr(III), which favors the subsequent immobilization of chromium salts.

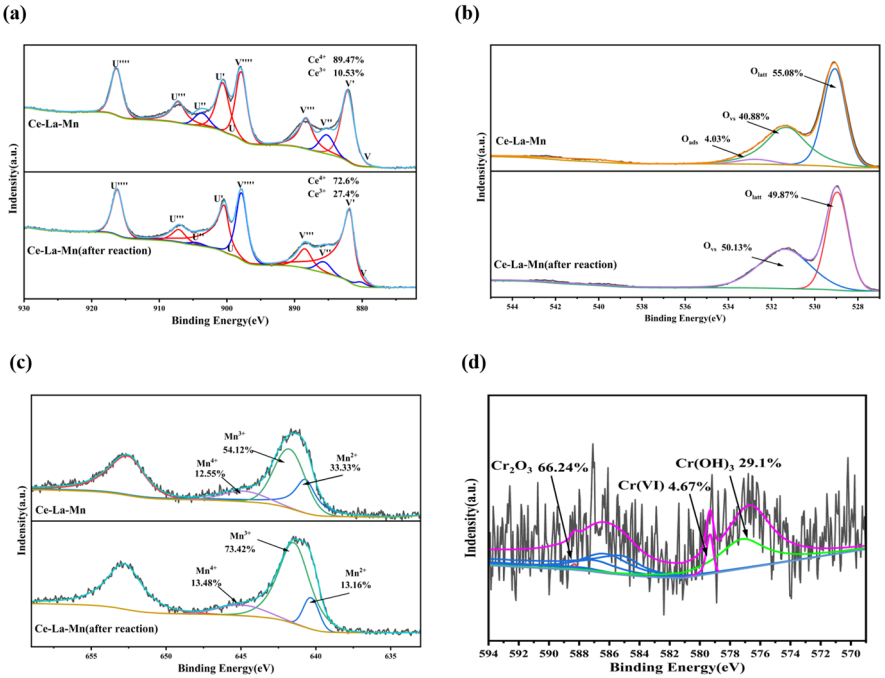

Figure 14. XPS spectra of Ce-La-Mn and Ce-La-Mn (after reaction): (**a**) Ce 3d; (**b**) O 1s; (**c**) Mn $2p_{3/2}$; (**d**) Cr 2p (Mode of occurrence of O, Cr, Ce and Mn in the reacted slag, respectively).

Figure 14d presents the XPS spectra of Cr 2p for the composite material before and after reaction. Through peak fitting based on Cr 2p, three forms of Cr were observed in the reacted composite material, including $Cr(OH)_3$ accounting for 29.1%, Cr_2O_3 accounting for 66.24%, and Cr(VI) accounting for 4.67%. These findings indicate that upon reaction, the majority of Cr(VI) has been reduced to Cr(III), with only a minor fraction of Cr(VI) being physically adsorbed onto the composite material. Compared to Ce-La-Pr, the elevated proportion of $Cr(OH)_3$ in Ce-La-Mn indicates a richer array of active sites, thereby promoting the formation of Cr(III)-OH- complexes during the reaction. This academic language underscores the enhanced reduction of Cr(VI) by Mn-doped Ce/La oxides and highlights the potential advantages of the composite material in chromium salt immobilization.

Based on previous analysis, we hypothesize a reaction mechanism for Ce-La-X(Mn/Pr)-O in removing Cr(VI) from aqueous solutions (Figure 15). Photocatalysis triggers Cr(VI) to cleave hydroxyl groups on the composite surface, inducing charge instability. This instability is stabilized by electron transfer, reducing Cr(VI) to the more stable Cr(III). The presence of Ce, La, and Ce(III) species likely enhances this reduction. Cr(VI) ultimately converts to Cr(III), which dissolves or adsorbs as $Cr(OH)_3$ on the composite surface. A minor fraction of Cr(VI) adsorbs directly onto active sites. The redox reaction can be schematically represented as follows:

$$\text{Ce-La-X(Mn/Pr)-O} + hv \rightarrow e^- + h^+ \quad (8)$$

$$H_2O + 2h^+ \rightarrow 1/2O_2 + 2H^+ \quad (9)$$

$$Cr_2O_7^{2-} + 14H^+ + 6e^- \rightarrow 2Cr^{3+} + 7H_2O \quad (10)$$

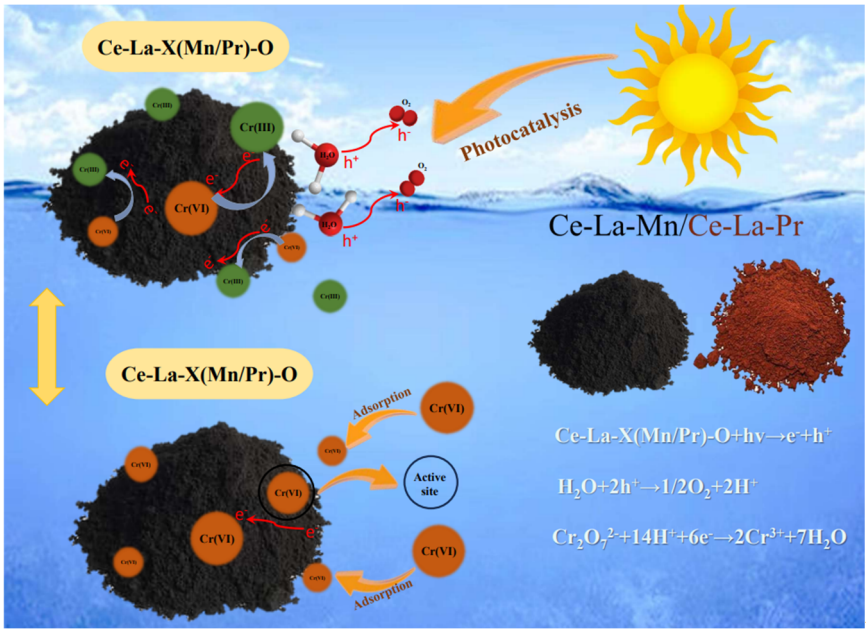

Figure 15. Proposed mechanisms for the interaction of Ce-La-X(Pr/Mn) and Cr(VI) in aqueous systems.

4. Conclusions

In this study, utilizing the co-precipitation method, we successfully fabricated a Ce-La-based multicomponent composite oxide optimized with a Ce:La:X(Mn/Pr) molar ratio of 0.72:0.18:0.1. The material was crystallized for 3 h and subsequently calcined at 500 °C for 4 h using ammonia as the precipitating agent. Under photocatalytic conditions, a mere 0.04 g of this composite exhibited remarkable Cr(VI) removal efficiency, achieving over 98% removal within 15 min from a 50 mL solution containing 20 mg/L Cr(VI). Notably, even after three cycles of use, the removal efficiency remained above 80%. The Ce-La-Mn composite oxide exhibited dual functionalities of reduction and adsorption, demonstrating exceptional performance in Cr(VI) removal. The introduction of photocatalysis significantly enhanced the reduction efficiency of Cr(VI) by the composite, while the doping of Mn profoundly augmented the interaction among metal elements. This interaction not only facilitated the generation of surface active centers on the Ce-La oxide, promoting in-situ "reduction–adsorption", but also bolstered the surface electron transport capacity and broadened the visible light absorption range of the Ce-La oxide, thereby facilitating the conversion of Cr(VI) to Cr(III). Unlike conventional Ce-La binary oxides, the Ce-La-Mn oxide did not exist as a mere mixture of Ce, La, and Mn oxides. Instead, the mutually doped oxides and Ce-La-Mn solid solutions synergistically enhanced the performance of Cr(VI) reduction and adsorption. This study offers a novel approach for the preparation of rare earth multi-component composite oxides and their efficient utilization in Cr(VI) removal.

Author Contributions: Conceptualization, X.F.; methodology, X.F. and Z.Y.; validation, Z.Y.; formal analysis X.F. and Z.Y.; investigation, X.F. and Z.Y.; resources, X.F.; data curation, X.F. and Z.Y.; writing—original draft, Z.Y.; writing—review and editing, X.F.; visualization, Z.Y.; supervision, X.F.; project administration, X.F.; funding acquisition, X.F. All authors have read and agreed to the published version of the manuscript.

Funding: The work was funded by the Major Innovation Program of Shandong Province (Shandong Provincial Department of Science and Technology), 2021CXGC011206.

Data Availability Statement: The data are not publicly available due to agency management. Data was obtained from China University of Mining and Technology and Jiangsu Yuankun Rare Earth Co., Ltd., and are available from the authors with the permission of China University of Mining and Technology and Jiangsu Yuankun Rare Earth Co., Ltd.

Conflicts of Interest: Xiujuan Feng was the majority shareholder of Jiangsu Yuankun Rare Earth Co., Ltd. Xiujuan Feng and Zebang Yu declare that the research was conducted in the absence of any commercial or financial relationships that could be construed as a potential conflict of interest.

References

1. Ramli, N.N.; Kurniawan, S.B.; Ighalo, J.O.; Said, N.S.M.; Marsidi, N.; Buhari, J.; Shah, R.A.R.; Zulkifli, M.; Alias, J.; Daud, N.M.; et al. A review of the treatment technologies for hexavalent chromium contaminated water. *BioMetals* **2023**, *36*, 1189–1219. [CrossRef] [PubMed]
2. Zhu, T.; Huang, W.; Zhang, L.; Gao, J.; Zhang, W. Adsorption of Cr(VI) on cerium immobilized cross-linked chitosan composite in single system and coexisted with Orange II in binary system. *Int. J. Biol. Macromol.* **2017**, *103*, 605–612. [CrossRef] [PubMed]
3. Saleem, M.H.; Afzal, J.; Rizwan, M.; Shah, Z.U.H.; Depar, N.; Usman, K. Chromium toxicity in plants: Consequences on growth, chromosomal behavior and mineral nutrient status. *Turk. J. Agric. For.* **2022**, *46*, 371–389. [CrossRef]
4. Naseri, A.; Asghari Sarabi, G.; Samadi, M.; Yousefi, M.; Ebrahimi, M.; Moshfegh, A.Z. Recent advances on dual-functional photocatalytic systems for combined removal of hazardous water pollutants and energy generation. *Res. Chem. Intermed.* **2022**, *48*, 911–933. [CrossRef]
5. Rosales, E.; Ferreira, L.; Angeles Sanroman, M.; Tavares, T.; Pazos, M. Enhanced selective metal adsorption on optimised agroforestry waste mixtures. *Bioresour. Technol.* **2015**, *182*, 41–49. [CrossRef] [PubMed]
6. Irshad, M.A.; Sattar, S.; Nawaz, R.; Al-Hussain, S.A.; Rizwan, M.; Bukhari, A.; Waseem, M.; Irfan, A.; Inam, A.; Zaki, M.E.A. Enhancing chromium removal and recovery from industrial wastewater using sustainable and efficient nanomaterial: A review. *Ecotoxicol. Environ. Saf.* **2023**, *263*, 115231. [CrossRef] [PubMed]
7. Ren, Y.; Lei, X.; Wang, H.; Xiao, J.; Qu, Z. Enhanced Catalytic Performance of La-Doped $CoMn_2O_4$ Catalysts by Regulating Oxygen Species Activity for VOCs Oxidation. *ACS Catal.* **2023**, *13*, 8293–8306. [CrossRef]
8. Yang, J.; Yang, S.; Zhang, J.; He, J.; Jiang, W. Photocatalytic treatment of Cr(VI) with ZrO_2 and application of by-products as ethane dehydrogenation catalyst. *Desalination Water Treat.* **2023**, *286*, 205–216. [CrossRef]
9. Atran, A.A.; Hamdy, M.S. Improving the Photocatalytic Performance of Porous Ceria under Visible Light Illumination *via* Mn Incorporation. *Catalysts* **2023**, *13*, 523. [CrossRef]
10. Li, J.; Liu, Q.; Huang, R.; Wang, G. Synthesis of a novel Ce(III)-incorporated cross-linked chitosan and its effective removal of fluoride from aqueous solution. *J. Rare Earths* **2016**, *34*, 1053–1061. [CrossRef]
11. Li, L.; Hu, S.-z.; Huang, T.; Zhang, N.; Wang, Y. Fabricating the ternary CeO_2@CNTs/CdSe composite with synchronously enhanced adsorption and photocatalytic activity toward water-soluble pollutants removal. *Chem. Eng. J.* **2023**, *476*, 146574. [CrossRef]
12. Meng, J.; He, M.; Li, F.; Li, T.; Huang, Z.; Cao, W. Combining Ce-metal-organic framework with CdS for efficient photocatalytic removals of heavy metal ion and organic pollutant under visible and solar lights. *Inorganica Chim. Acta* **2023**, *557*, 121701. [CrossRef]
13. Wang, Q.; Cui, M.; Huang, X.; Hou, Y.; Yue, M.; Zhong, Q.; Zhang, Y. The effect of hydrogen peroxide on properties of $Ce_{0.35}Zr_{0.55}La_{0.055}Pr_{0.045}O_2$ oxides and the catalytic performance used on Pd supported three-way catalyst. *J. Rare Earths* **2017**, *35*, 1092–1101. [CrossRef]
14. Jaramillo-Fierro, X.; Cuenca, G.; Ramon, J. Comparative Study of the Effect of Doping $ZnTiO_3$ with Rare Earths (La and Ce) on the Adsorption and Photodegradation of Cyanide in Aqueous Systems. *Int. J. Mol. Sci.* **2023**, *24*, 3780. [CrossRef] [PubMed]
15. He, Y.; Zhong, D.; Xu, Y.; Zhang, J.; Jiang, R.; Liao, P. Preparation of La-doped Ti/SnO_2-Sb_2O_4 anode and its electrochemical oxidation performance of rhodamine B. *Environ. Sci. Pollut. Res.* **2024**, *31*, 21632–21645. [CrossRef] [PubMed]
16. Yi, Y.; Fu, Y.; Wang, Y.; Xu, Z.; Diao, Z. Lanthanum/iron co-modified biochar for highly efficient adsorption of low-concentration phosphate from aqueous solution. *J. Environ. Chem. Eng.* **2024**, *12*, 111876. [CrossRef]
17. Zhang, P.; He, M.; Xu, Z.; Li, F.; Fang, D.; Li, C.; Lv, C.; Mo, X.; Li, K.; Wang, H. Incorporation of edge-N into La-doped hierarchical carbon framework enables high-efficiency phosphate electrosorption: Boosting accessible active centers and bridging charge transfer paths. *Chem. Eng. J.* **2024**, *481*, 148518. [CrossRef]
18. Jin, H.-G.; Gu, J.-X.; Lin, W.; Xu, W.-J.; Huang, B.-X.; Yang, F.; Wen, J.-X.; Ren, Y.; Chao, Z.-S. Room temperature aqueous synthesis of Ce(IV)-MOFs with UiO-66 architecture and their photocatalytic decarboxylative oxygenation of arylacetic acids. *Microporous Mesoporous Mater.* **2022**, *346*, 112257. [CrossRef]
19. Kalidasan, K.; Mallapur, S.; Munirathnam, K.; Nagarajaiah, H.; Reddy, M.B.M.; Kakarla, R.R.; Raghu, A.V. Transition metals-doped g-C3N4 nanostructures as advanced photocatalysts for energy and environmental applications. *Chemosphere* **2024**, *352*, 141354. [CrossRef]
20. Arulkumar, E.; Shree, S.S.; Thanikaikarasan, S. Synthesis and characterization of CuO-Mn_3O_4: Application to chromium (VI) photocatalytic reduction. *J. Mater. Sci.-Mater. Electron.* **2024**, *35*, 198. [CrossRef]
21. Mjahed, M.; Bouda, H.; Salmani, E.; Zahraouy, H.E.; Benyoussef, A. Impact of rare earth (La, Pr, Eu) impurities on the perovskite $SrTiO_3$ for efficient photocatalytic activity. *Phys. Scr.* **2024**, *99*, 025916. [CrossRef]
22. Mikolajczyk, A.; Wyrzykowska, E.; Mazierski, P.; Grzyb, T.; Wei, Z.; Kowalska, E.; Caicedo, P.N.A.; Zaleska-Medynska, A.; Puzyn, T.; Nadolna, J. Visible-light photocatalytic activity of rare-earth-metal-doped TiO_2: Experimental analysis and machine learning for virtual design. *Appl. Catal. B-Environ. Energy* **2024**, *346*, 123744. [CrossRef]

23. Li, Q.; He, S.; Wang, L.; Zhao, M.; Guo, T.; Ma, X.; Meng, Z. A novel Z-scheme heterojunction g-C_3N_4/g-C_3N_4/Pr_6O_{11} for efficient visible-light photocatalytic degradation of sulfonamide. *Appl. Organomet. Chem.* **2024**, *38*, e7344. [CrossRef]
24. Wu, L.; Zhang, G.; Tang, D. A novel high efficient Mg-Ce-La adsorbent for fluoride removal: Kinetics, thermodynamics and reusability. *Desalination Water Treat.* **2016**, *57*, 23844–23855. [CrossRef]
25. Choi, Y.-B.; Kim, B.-G.; Son, J.-H.; Jung, Y.-G. Synthesis, characteristics, and redox properties of Zr/Sn-doped CeO_2 nanoparticles in H_2 gas at high temperatures. *Ceram. Int.* **2019**, *45*, 12983–12988. [CrossRef]
26. Zhang, K.; Yu, G.; Zhao, H.; Wang, H.; Zhang, G.; Chen, Y. Preparation, characterisation and catalytic property of ultrafine Ce-La-Mn mixed oxides. *J. Exp. Nanosci.* **2012**, *7*, 233–242. [CrossRef]
27. Wang, Y.; Deng, W.; Wang, Y.; Guo, L.; Ishihara, T. A comparative study of the catalytic oxidation of chlorobenzene and toluene over Ce-Mn oxides. *Mol. Catal.* **2018**, *459*, 61–70. [CrossRef]
28. Liu, J.; Wang, T.; Shi, N.; Yang, J.; Serageldin, M.A.; Pan, W.-P. Enhancing the interaction between Mn and Ce oxides supported on fly ash with organic acid ligands interface modification for effective VOC removal: A combined experimental and DFT plus U study. *Fuel* **2022**, *313*, 123043. [CrossRef]
29. Andana, T.; Rappé, K.G.; Nelson, N.C.; Gao, F.; Wang, Y. Selective catalytic reduction of NOx with NH_3 over Ce-Mn oxide and Cu-SSZ-13 composite catalysts—Low temperature enhancement. *Appl. Catal. B Environ.* **2022**, *316*, 121522. [CrossRef]
30. Ji, Y.; Ding, B.; Ni, W.; Li, X.; He, X.; Chen, Z.; Ran, S.; Lu, H. Tailoring the crystal structure of $CaTiO_3$ by multielement doping for photo-assisted activation of NO. *Chem. Eng. J.* **2022**, *450*, 138255. [CrossRef]
31. Li, P.; Zhang, W.; Zhang, X.; Wang, Z.; Wang, X.; Ran, S.; Lv, Y. Synthesis, Characterization, and Photocatalytic Properties of Flower-like Mn-doped Ceria. *Mater. Res.* **2018**, *21*, e20180167. [CrossRef]
32. Meena, S.; Anantharaju, K.S.; Vidya, Y.S.; Renuka, L.; Uma, B.; Sharma, S.C.; Prasad, B.D.; More, S.S. Enhanced sunlight driven photocatalytic activity and electrochemical sensing properties of Ce-doped $MnFe_2O_4$ nano magnetic ferrites. *Ceram. Int.* **2021**, *47*, 14760–14774. [CrossRef]
33. Lu, M.; Su, Z.; Zhang, Y.; Zhang, H.; Wang, J.; Li, Q.; Jiang, T. Mn-Doped Spinel for Removing Cr(VI) from Aqueous Solutions: Adsorption Characteristics and Mechanisms. *Materials* **2023**, *16*, 1553. [CrossRef] [PubMed]
34. Afroze, S.; Sen, T.K. A Review on Heavy Metal Ions and Dye Adsorption from Water by Agricultural Solid Waste Adsorbents. *Water Air Soil Pollut.* **2018**, *229*, 225. [CrossRef]
35. Cui, Y.W.; Li, J.; Du, Z.F.; Peng, Y.Z. Cr(VI) Adsorption on Red Mud Modified by Lanthanum: Performance, Kinetics and Mechanisms. *PLoS ONE* **2016**, *11*, e0161780. [CrossRef]
36. Luo, Z.; Zhu, Z. Effects of Support Preparation Methods on Structural and Catalytic Properties of Au/MnO_x-CeO_2. *Catal. Lett.* **2023**, *154*, 422–429. [CrossRef]
37. Al-Bassami, N.S.; Mansour, S.F.; Abdel-Fattah, E.; Abdo, M.A. Ce-Co-Mn-Zn ferrite nano catalyst: A synergetic effect of rare earth Ce^{3+} on enhanced optical properties and photocatalysis. *Ceram. Int.* **2023**, *49*, 20601–20612. [CrossRef]
38. Wang, S.; Chen, C.; Li, Y.; Zhang, Q.; Li, Y.; Gao, H. Synergistic Effects of Optical and Photoluminescence Properties, Charge Transfer, and Photocatalytic Activity in $MgAl_2O_4$Ce and Mn-Codoped $MgAl_2O_4$Ce Phosphors. *J. Electron. Mater.* **2019**, *48*, 6675–6685. [CrossRef]
39. Zhao, D.; Cai, C. Cerium-based UiO-66 metal-organic framework for synergistic dye adsorption and photodegradation: A discussion of the mechanism. *Dye. Pigment.* **2021**, *185*, 108957. [CrossRef]
40. Wang, J.; Liang, Y.; Jin, Q.; Hou, J.; Liu, B.; Li, X.; Chen, W.; Hayat, T.; Alsaedi, A.; Wang, X. Simultaneous Removal of Graphene Oxide and Chromium(VI) on the Rare Earth Doped Titanium Dioxide Coated Carbon Sphere Composites. *ACS Sustain. Chem. Eng.* **2017**, *5*, 5550–5561. [CrossRef]
41. Wen, Z.; Zhang, Y.; Cheng, G.; Wang, Y.; Chen, R. Simultaneous removal of As(V)/Cr(VI) and acid orange 7 (AO7) by nanosized ordered magnetic mesoporous Fe-Ce bimetal oxides: Behavior and mechanism. *Chemosphere* **2019**, *218*, 1002–1013. [CrossRef] [PubMed]
42. Zuo, K.; Huang, X.; Liu, X.; Garcia, E.M.G.; Kim, J.; Jain, A.; Chen, L.; Liang, P.; Zepeda, A.; Verduzco, R.; et al. A Hybrid Metal-Organic Framework-Reduced Graphene Oxide Nanomaterial for Selective Removal of Chromate from Water in an Electrochemical Process. *Environ. Sci. Technol.* **2020**, *54*, 13322–13332. [CrossRef] [PubMed]
43. Tao, R.; Li, H.; Liu, Z.; Zhang, X.; Wang, M.; Shen, W.; Qu, M.; Mei, Y. The adsorbent preparation of FeOOH@PU for effective chromium (VI) removal. *Environ. Sci. Pollut. Res.* **2023**, *30*, 33160–33169. [CrossRef]
44. Asuha, S.; Zhou, X.G.; Zhao, S. Adsorption of methyl orange and Cr(VI) on mesoporous TiO_2 prepared by hydrothermal method. *J. Hazard. Mater.* **2010**, *181*, 204–210. [CrossRef] [PubMed]
45. Hu, B.; Wu, L.; Ou, M.; Wang, X.; Tang, Y. Sorption Studies of Chromium(VI) onto Cerium/Ferroferric Oxide Composites. *J. Inorg. Organomet. Polym. Mater.* **2021**, *31*, 2627–2637. [CrossRef]
46. Nelson, N.C.; Andana, T.; Rappé, K.G.; Wang, Y. Mechanistic insight into low temperature SCR by ceria-manganese mixed oxides incorporated into zeolites. *Catal. Sci. Technol.* **2023**, *13*, 1111–1118. [CrossRef]